ADVANCED FUNCTIONAL MATERIALS
www.afm-journal.de

Proximity-Induced Fully Ferromagnetic Order with Eightfold Magnetic Anisotropy in Heavy Transition Metal Oxide $CaRuO_3$

Jine Zhang, Xiaobing Chen, Mengqin Wang, Qinghua Zhang, Wenxiao Shi, Xiaozhi Zhan, Meng Zhao, Zhe Li, Jie Zheng, Hui Zhang, Furong Han, Huaiwen Yang, Tao Zhu, Banggui Liu, Fengxia Hu, Baogen Shen, Yuansha Chen, Yue Zhang,* Yunzhong Chen,* Weisheng Zhao,* and Jirong Sun**

Ferromagnetic materials with a strong spin-orbit coupling (SOC) have attracted much attention in recent years because of their exotic properties and potential applications in energy-efficient spintronics. However, such materials are scarce in nature. Here, a proximity-induced paramagnetic to ferromagnetic transition for the heavy transition metal oxide $CaRuO_3$ in (001)-($LaMnO_3$/$CaRuO_3$) superlattices is reported. Anomalous Hall effect is observed in the temperature range up to 180 K. Maximal anomalous Hall conductivity and anomalous Hall angle are as large as ∼15 Ω^{-1} cm^{-1} and ∼0.93%, respectively, by one to two orders of magnitude larger than those of the typical 3d ferromagnetic oxides such as $La_{0.67}Sr_{0.33}MnO_3$. Density functional theory calculations indicate the existence of avoid band crossings in the electronic band structure of the ferromagnetic CRO layer, which enhances Berry curvature thus strong anomalous Hall effects. Further evidences from polarized neutron reflectometry show that the $CaRuO_3$ layers are in a fully ferromagnetic state (∼0.8 μ_B/Ru), in sharp contrast to the proximity-induced canted antiferromagnetic state in 5d oxides $SrIrO_3$ and $CaIrO_3$ (∼0.1 μ_B/Ir). More than that, the magnetic anisotropy of the (001)-($LaMnO_3$/$CaRuO_3$) superlattices is eightfold symmetric, showing potential applications in the technology of multistate data storage.

1. Introduction

One of the central issues of spintronics is the electric switching of the direction of perpendicular magnetization via spin-orbit torque, without an auxiliary magnetic field which makes the device complex and power-consuming. Recently, it is reported that the field-free switching can be realized via a ferromagnetic (FM) material with strong spin-orbit coupling (SOC).[1–4] In this case, the polarization direction of the spin current suffers from the manipulation of magnetization and thus can be *z*-axis-directed, enabling an efficient field-free electric switching of magnetization.

However, metallic materials simultaneously owning FM order and strong SOC are scarce. Although it is easy to find FM 3d transition metal oxides, the SOC of these oxides is generally weak. 4d and 5d transition metal oxides exhibit a strong SOC but they are usually paramagnetic (PM), due to weak electron correlation between

J. Zhang, M. Zhao, H. Zhang, F. Han, H. Yang, Y. Zhang, W. Zhao
School of Integrated Circuit Science and Engineering
Beihang University
Beijing 100191, China
E-mail: yz@buaa.edu.cn; weisheng.zhao@buaa.edu.cn

J. Zhang, M. Wang, Q. Zhang, W. Shi, Z. Li, J. Zheng, T. Zhu, B. Liu, F. Hu, B. Shen, Y. Chen, Y. Chen, J. Sun
Beijing National Laboratory for Condensed Matter Physics and Institute of Physics
Chinese Academy of Sciences
Beijing 100190, China
E-mail: yschen@iphy.ac.cn; yzchen@iphy.ac.cn; jrsun@iphy.ac.cn

X. Chen
Shenzhen Institute for Quantum Science and Engineering and Department of Physics
Southern University of Science and Technology
Shenzhen 518055, China

The ORCID identification number(s) for the author(s) of this article can be found under https://doi.org/10.1002/adfm.202306434

M. Wang, W. Shi, Z. Li, J. Zheng, F. Hu, B. Shen, Y. Chen, J. Sun
School of Physical Sciences
University of Chinese Academy of Sciences
Beijing 100049, China

X. Zhan, T. Zhu
Spallation Neutron Source Science Center
Dongguan 523803, China

F. Hu, J. Sun
Songshan Lake Materials Laboratory
Dongguan, Guangdong 523808, China

B. Shen
Ningbo Institute of Materials Technology & Engineering
Chinese Academy of Sciences
Ningbo, Zhejiang 315201, China

Y. Chen
Fujian Innovation Academy
Chinese Academy of Sciences
Fuzhou, Fujian 350108, China

DOI: 10.1002/adfm.202306434

extended orbits, or antiferromagnetic. In fact, $SrRuO_3$ may be the only metallic oxide showing FM order and strong SOC, though its Curie temperature is relatively low (~150 K).[5–9] Therefore, new materials which allow an efficient electric manipulation of magnetization are highly desired.

As well documented, the strongly entangled multiple degrees of freedom in complex oxides can be dramatically tuned by interface engineering, leading to emergent phenomena.[10] Therefore, constructing heterostructures or superlattices with different complex oxides provides a fertile field for the generation of the electronic and magnetic ground states that are unavailable in bulk oxides.[11–18] In fact, extensive efforts have been devoted to modifying the ground state of $SrIrO_3$, a PM semimetal with a strong SOC. Due to Dzyaloshinskii-Moriya interaction, unfortunately, a canted antiferromagnetic rather than a collinear FM order establishes in the $SrIrO_3$ layer of the $La_{0.67}Sr_{0.33}MnO_3/SrIrO_3$,[19–22] $LaMnO_3/SrIrO_3$,[23] $LaCoO_3/SrIrO_3$,[24] and $SrMnO_3/SrIrO_3$[25–26] heterostructures, with a net magnetic moment of only ~0.1 μ_B/Ir. $CaIrO_3$-based heterostructures such as $CaMnO_3/CaIrO_3$[27–29] and $SrTiO_3/CaIrO_3$[30] were also investigated, and it is unsuccessful either to induce a collinear FM order in the $CaIrO_3$ layer. Obviously, it remains challenging to get materials with a collinear FM order and a strong SOC.

PM $CaRuO_3$ (CRO) is a 4d transition metal oxide with a strong SOC (~0.15 eV) that is comparable to electron correlation.[31–32] It is in a balanced state of strongly competitive mechanisms and thus is sensitive to external perturbations such as the proximity effect from a FM neighbor. 3d transition metal oxide $LaMnO_3$ (LMO) film is a typical FM insulator with a large magnetic moment (4 μ_B/Mn).[33] Here we report on a proximity-driven PM to FM transition for the CRO layers of the (001)-(LMO_{18}/CRO_n) superlattices (n = 4, 6, 8, and 10 unit cells). Anomalous Hall effect (AHE), which is strong at low temperatures and remains sizable up to 180 K, indicates the establishment of an FM order in the CRO layer. The maximal anomalous Hall conductivity is as large as 15 Ω^{-1} cm^{-1} and anomalous Hall angle is as high as ~0.93%. Further evidences from polarized neutron reflectometry (PNR) indicate the appearance of a collinear FM order, with a saturation magnetization of ~0.8 μ_B/Ru. More than that, the (001)-(LMO_{18}/CRO_n) superlattices show an eight-fold symmetric magnetic anisotropy (MA) though the MA of the (001)-LMO bare layer is uniaxial.

2. Results and Discussions

2.1. Structural Analysis

$(LMO_{18}/CRO_n)_8$ superlattices (SLs) composed of alternately stacked LMO and CRO layers were epitaxially grown on (001)-oriented $(LaAlO_3)_{0.3}(SrAl_{0.5}Ta_{0.5}O_3)_{0.7}$ (LSAT) substrates by pulsed laser deposition. Layer thickness was fixed to 18 unit cells for LMO and varied from n = 4, 6, 8, to 10 unit cells for CRO (Figure S1 of supporting information). The repetition of the SLs is 8. Please refer to the experimental section for detailed procedures for sample preparation. **Figure 1**a shows the X-ray diffraction (XRD) spectra of the SLs. In addition to the (001) main peak, satellite peaks up to three levels are clearly seen, indicating the high quality of the SLs with targeted structures. As for the shift of the satellite peak toward main peak as the layer thickness of CRO increases, it is a typical feature of the XRD spectra of the SLs. To determine the in-Plane strain state of the SLs, reciprocal space mapping (RSM) of the $(\bar{1}03)$ reflection is collected for two typical SLs of $(LMO_{18}/CRO_4)_8$ (Figure 1b) and $(LMO_{18}/CRO_8)_8$ (Figure 1c). The diffraction spot of the SLs locates just below that of LSAT, i.e., the SLs are coherently strained to the substrate, without lattice relaxation. This conclusion is applicable to all samples (Figure S1 of supporting information). According to this analysis, the in-plane lattice parameter of the SLs is ~3.87 Å, a lattice constant of the LSAT. Therefore, the strain state is tensile for the CRO layer and compressive for the LMO layer. Notably, bulk CRO, LMO, and LSAT show lattice parameters of ~3.85 Å, ~3.90 Å, and ~3.87 Å, respectively.

To get the information about atomic scale structure, the lattice image of $(LMO_{18}/CRO_6)_8$ is collected by high-resolution scanning transmission electron microscope (STEM) with double C_S correctors. Figure 1d presents the high-angle annular dark-field (HAADF) image of the cross-section of $(LMO_{18}/CRO_6)_8$, recorded along $[\bar{1}10]$ zone axis. Due to different color contrast, the LMO and CRO layer can be easily identified. As expected, the LMO and CRO layer alternately stack along the vertical direction, showing a high-quality epitaxial growth. A further line profile analysis of the atomic contrast along the vertical direction indicates that the LMO/CRO interface is atomically sharp, without interlayer mixing. In contrast, partial Ca^{2+} ions in the first Ca–O layer at the CRO/LMO interface are replaced by La^{3+} ions, resulting in an A-site intermixing within one unit cell.

2.2. Emergent Ferromagnetism in CRO Induced by Proximity Effect

To explore the effect of interface engineering, we investigated the electronic transport properties of the $(LMO_{18}/CRO_n)_8$ SLs with the standard four-probe technique. **Figure 2**a shows the longitudinal resistivity ρ_{xx} of the SLs, as a function of temperature. Results of a bare LMO film (~56 nm in thickness) and a bare CRO film (~10 nm in thickness) are also presented for comparison. With the decrease of temperature ρ_{xx} of the SLs exhibits first a slow decrease in a broad temperature range and then a sizable upturn that is absent in the bare CRO film; weak localization may take place at low temperatures in ultrathin CRO layers due to enhanced interfacial scattering. Notably, the transport behavior of the SLs should be solely determined by the CRO layers since the resistivity of the LMO layers is more than four orders of magnitude greater than that of the SLs. With the decrease of the CRO layer thickness, the SLs exhibit an overall growth in resistivity and, simultaneously, a crossover from metal-like to semiconductor-like behavior. Semiconducting behavior prevails in the SLs of n = 4 unit cells. It may be a distinct property of the interfacial CRO layer; the interfacial effects in this sample should be the strongest among all samples investigated here. Inset plot in Figure 2a is a close view of the ρ_{xx}-T relation presented in double logarithm scale. At first glance, $\log(\rho_{xx})$ is linearly

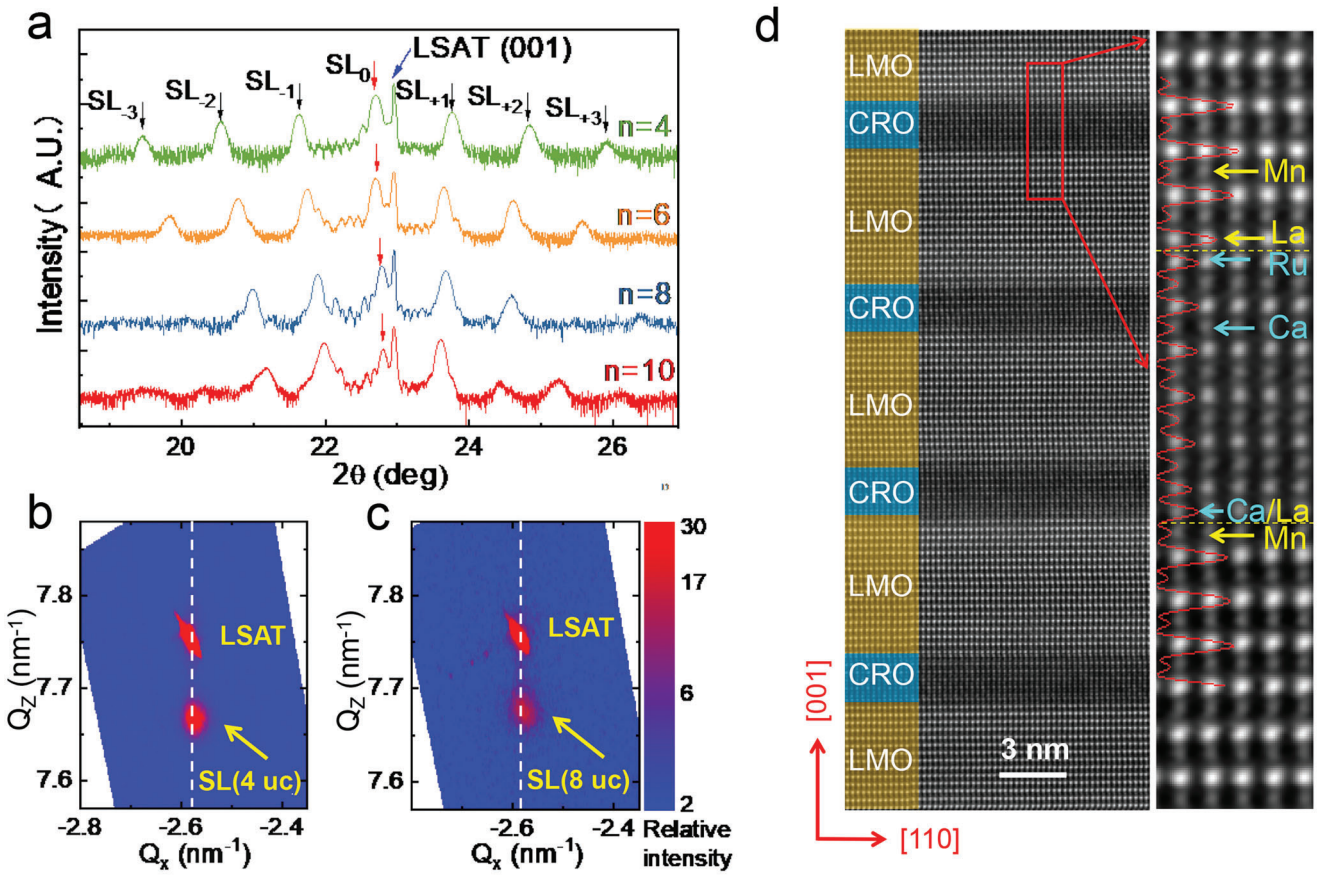

Figure 1. Structure characterization. a) XRD patterns for $(LMO_{18}/CRO_n)_8$ SLs on LSAT. SL_0 indicates (001) main peak and SL_{-3}, SL_{-2}, SL_{-1}, SL_{+1}, SL_{+2}, SL_{+3} indicate satellite peaks. b-c) Typical RSM of the $(\bar{1}03)$ reflections for $(LMO_{18}/CRO_n)_8$ SLs with $n = 4$ (b) and $n = 8$ (c). d) High-angle annular dark-field (HAADF) image of the cross-section of the $(LMO_{18}/CRO_6)_8$ SLs, recorded along $[1\bar{1}0]$ zone axis. The LMO and CRO sublayers are marked by yellow and blue color. The right panel is the enlarged image.

dependent on -log(T) above 75 K. However, a careful analysis indicates a deviation from linearity above ~200 K. As will be seen later, 200 K is the transition temperature from FM to PM state for the CRO layers. Above 200 K, we found a linear $\rho_{xx} \sim$ -log(T) relation (Figure S2 of supporting information). This is a signature of spin flip scattering.[24] However, why the FM ordering results in a linear log(ρ_{xx}) ~- log(T) relation below 200 K is unclear at present.

Anomalous Hall effect (AHE) is a fingerprint of FM order, appearing in materials with broken time-reversal symmetry and SOC. It is usually adopted to assess the FM order. Figure 2b shows the anomalous Hall resistivity measured at different temperatures for the typical SL of $(LMO_{18}/CRO_4)_8$. Strong AHE appears at low temperatures, showing clear ρ_{xy}-H hysteresis loops while cycling magnetic field. The maximal saturation Hall resistivity is $\rho_{xy}^{AHE} \sim 12.4$ (μΩ cm), appearing at 2 K. The corresponding anomalous Hall angle is ~0.93%, defined by the ratio $\rho_{xy}^{AHE}/\rho_{xx}$. This value is two orders of magnitude larger than that of 3d oxide $La_{2/3}Sr_{1/3}MnO_3$ (0.002%–0.01%),[34] comparable to that of 5d iridate oxide (0.8%).[24] With the increase of temperature, the Hall resistivity decreases smoothly whereas the ρ_{xy}-H loop shrinks rapidly. Magnetic hysteresis disappears above 50 K but the AHE remains visible up to 180 K. Such a hysteretic behavior can be well-fitted by a modified Heaviside step function

$$\rho_{xy}^{AHE} = R_s \cdot M_s \cdot \tanh\left[h \cdot \left(H \pm H_c\right)\right] \quad (1)$$

where the R_S, M_S, h, and H_C are the AHE coefficient, the saturation magnetization, the slope at H_C, and the coercive field, respectively. These results strongly suggest the appearance of long-range FM order in the CRO layers which dominates the transport behavior of the SLs as mentioned above. Inset plot in Figure 2b depicts the saturation Hall resistivity (ρ_{xy}^{AHE}) as a function of temperature. Based on this figure the critical temperature for FM ordering can be deduced, and it is ~200 K. Notably, 200 K is also the temperature where transport anomaly appears (inset plot in Figure 2a).

The ferromagnetism is a general property of the SLs investigated here. Figure 2c shows the ρ_{xy}-H curves for the SLs with different CRO layers, obtained at $T = 2$ K. The SL with the thinnest CRO layer ($n = 4$ unit cells) exhibits the largest Hall resistivity. With the increase of the layer thickness of CRO, ρ_{xy}^{AHE} displays a monotonic decrease. However, it remains sizable when $n =$ 10 unit cells ($\rho_{xy}^{AHE} \sim 1.7$ μΩ cm), the thickest CRO layer in our

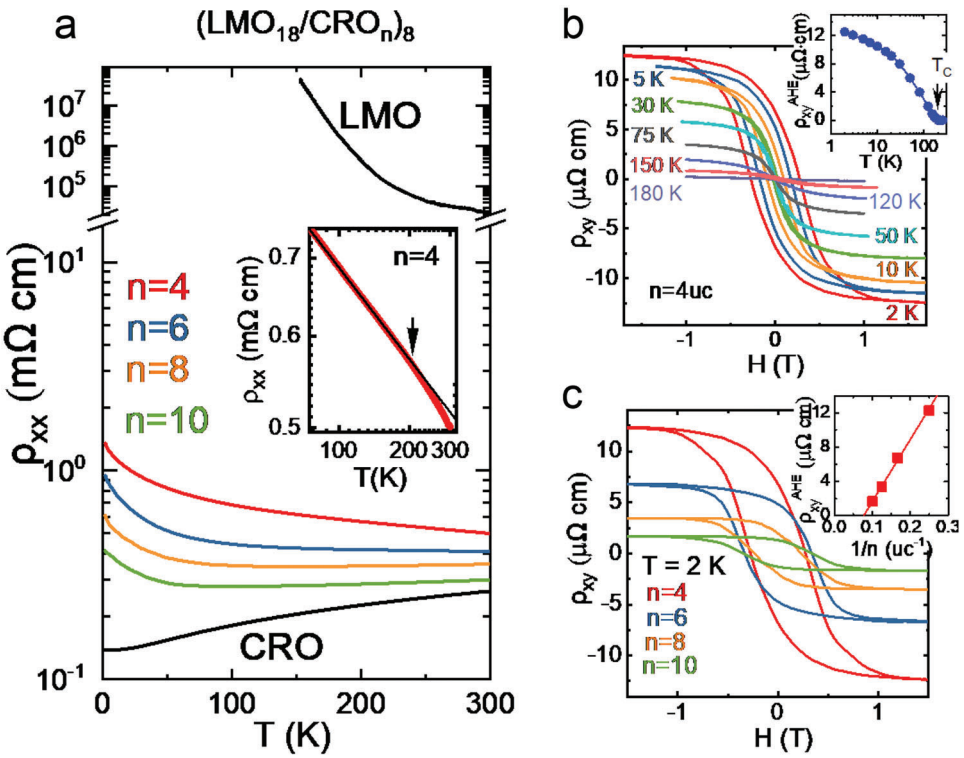

Figure 2. Transport properties. a) ρ_{xx}-T curves for $(LMO_{18}/CRO_n)_8$ SLs, CRO/LSAT, and LMO/LSAT films. b) ρ_{xy}-H curves for $(LMO_{18}/CRO_4)_8$ SLs measured at 2 K to 180 K. c) ρ_{xy}-H curves of the $(LMO_{18}/CRO_n)_8$ SLs with n = 4, 6, 8, and 10, measured at 2 K.

samples. Further analysis shows a linear dependence of ρ_{xy}^{AHE} on $1/n$ (inset plot in Figure 2c). This is a fingerprint of interfacial effect, i.e., the FM order establishes in the near interface region of CRO. Presumably, the interfacial layer of CRO is magnetized by the proximity effect of the LMO layer. This explains why it shows a similar Curie temperature with the LMO layer.[16]

To get a general idea about the AHE caused by interface engineering, in Figure S3 of supporting information we show the saturation anomalous Hall conductivity σ_{xy}^{AHE} as a function of longitudinal conductivity σ_{xx} for all SLs, where $\sigma_{xy}^{AHE} = \rho_{xy}^{AHE}/\rho_{xx}^2$. Data of representative magnetic oxides are also presented for comparison. The SL samples located near the border of poorly conducting and moderately dirty regimes.[35,36] The maximal Hall conductivity is ~15 Ω^{-1} cm^{-1}, obtained at 30 K for the $(LMO_{18}/CRO_6)_8$ SL. This value is much larger than that of $La_{2/3}Sr_{1/3}MnO_3$ and $La_{1-x}Ca_xMnO_3$ (0.003~1 Ω^{-1} cm^{-1}),[34,37,38] $SrIrO_3$ and $CaIrO_3$ with a canted antiferromagnetic order induced by interface engineering (~3 Ω^{-1} cm^{-1} and 0.02 Ω^{-1} cm^{-1}).[24,28]

A deep understanding of the large σ_{xy}^{AHE} of the FM CRO layers can be got from DFT calculations. Details of the calculations are explained in Note 1 of the supporting information. Figure S4 in supporting Information compares the band structures for the FM ground state of CRO without and with SOC. Since the space group of CRO is Pnma, the nonzero Berry curvature $\Omega_z(k)$ is forbidden in nonmagnetic phase. When the FM CRO phase emerges, the time reversal is broken and the $\Omega_z(k)$ is no more zero. More importantly, we find the coexistence of FM order and SOC in CRO will result in avoiding band crossings in the band structure, opening small gaps by spin-orbit interaction as marked by circles in Figure S4b, Supporting Information. Most of these avoid band crossings exist within an energy range of −0.2 to 0.2 eV around the Fermi level, leading to the peak positions of $\Omega_z(k)$ as shown in Figure S4c, Supporting Information. As a result, the intrinsic AHE, which is determined by the integration of the Berry curvature $\Omega_z(k)$ over all the occupied bands in the entire Brillouin zone, has increased substantially. The calculated intrinsic σ_{xy}^{AHE}at at Fermi energy is up to ~63 Ω^{-1} cm^{-1} (Figure S4e, Supporting Information). The discrepancy between theoretical and experimental results indicates a space to improve the experimental AHE, which is possible by depressing interfacial scattering.

We also measured the magnetoresistance (MR) of the $(LMO_{18}/CRO_n)_8$ SLs. **Figure 3**c shows the MR obtained at T = 2 K by cycling the magnetic field along the normal direction of the film. Butterfly-shaped MR-H loops with two peaks at $\pm H_C$ are clearly seen, confirming the establishment of the FM order in the CRO layers. It is the field-induced rearrangement of magnetic domains around H_C that results in the complex relation between MR and H. This phenomenon is observed in all SLs though detailed features vary from sample to sample. A further analysis finds an equation that well reproduces the MR-H dependence

$$MR = -a^2 \ln\left(1 + b^2 H^2\right) - cM_S^2 \quad (2)$$

where a, b, and c are adjustable parameters, and M_S is the saturation magnetization deduced from the fitting of AHE curve

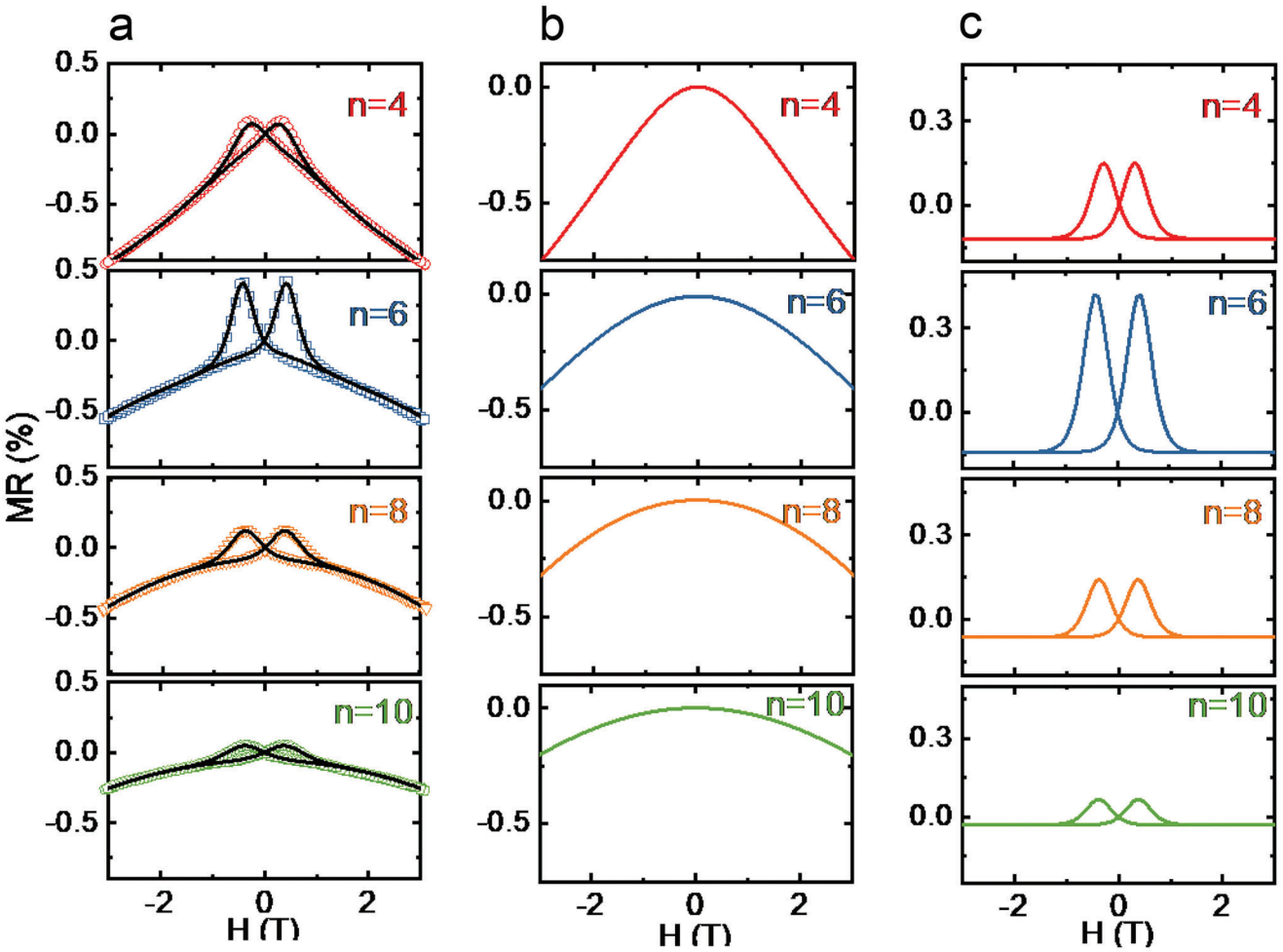

Figure 3. MR as a function of a magnetic field. a) MR-H curves for $(LMO_{18}/CRO_n)_8$ SLs with n = 4, 6, 8, and 10, measured at 2 K. Hollow symbols are experiment results. Black solid lines are the results of curve fitting, adopting Equation (2). b) MR contributed by short-range magnetic order. c) MR contributed by long-range magnetic order.

using Equation 1. The first term $-a^2\ln(1+b^2H^2)$ simulates the background of the MR, arising from the magnetic scattering of isolated moments.[39–42] Its emergence hints at the formation of short-range magnetic order. The second term $-cM_S^2$ captures the main feature of the effect of spin-flip scattering, mimicking the butterfly-shaped MR-H curves.[43] Figure 3b,c shows the two components that compose of the MR. The magnitude of the first component exhibits a smooth growth with the applied field, without signatures of saturation up to 3 T. This is understandable since aligning isolated magnetic moments is much more difficult. The second component exhibits a butterfly-shaped behavior under fairly low magnetic fields and a flat background when a magnetic field is high. This is the typical feature of the MR-H curve of the FM materials. The peak MR is ~0.27%, ~0.56%, ~0.20%, and ~0.10% for the samples of n = 4, 6, 8, and 10 unit cells, respectively. The SLs with n = 6 unit cells exhibit the maximal MR. The FM order of this sample may be more perfect. From 6 to 8 and to 10 unit cells, MR experiences a rapid decrease, indicating a degradation of the FM order in the samples with thick CRO layers. As indicated by the AHE analysis, proximity-induced ferromagnetism is an interface effect, appearing only in the near interface region of CRO. If each LMO layer drives a m-unit-cell-thick CRO layer into the FM state, the two LMO layers that sandwich CRO will yield a $2m$-unit-cell-thick FM CRO layer. When the CRO layer of the SLs is thicker than $2m$ unit cells, the intermediate region of it will remain PM. In this case, the MR will be shorted by the PM metallic CRO, exhibiting a decrease. This may be the case we see in the samples of n = 8 and 10 unit cells. Based on this analysis, we get a conclusion that the thickness of the magnetic layer adjacent to each LMO layer is thinner than 4 unit cells. As for the low MR in the sample of n = 4 unit cells, it can be ascribed to the low dimensionality of the ultrathin CRO layer, which disfavors long-range ferromagnetic order.[44] This inference is supported by the formation of short-range magnetic order in this sample, which produces a large background MR.

2.3. Spacially-Resoveled Magnetic Characterization and Theoretical Analysis

To clarify the depth profile of the magnetization across the SLs, we performed the measurements of polarized neutron

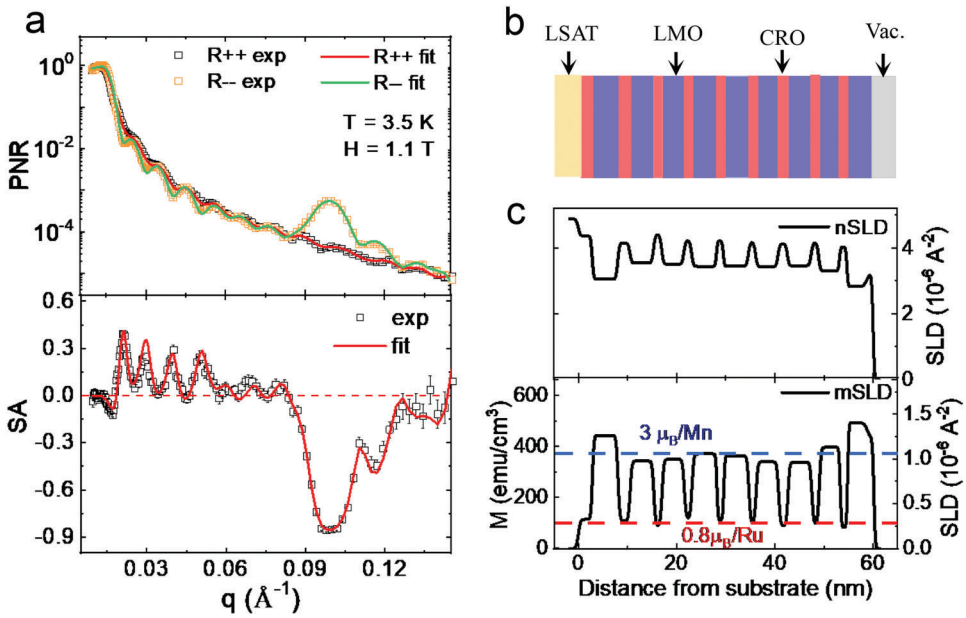

Figure 4. Magnetization depth profiles of the $[(LMO)_{18}/(CRO)_5]_9$ superlattice. a) Reflectivity curves for spin-up (R^{++}) and spin-down (R^{--}) polarized neutrons (upper panel), normalized to the asymptotic value of the Fresnel reflectivity ($R_F = 16\pi^2/q^4$). The measurements were performed at 3.5K in an applied in-plane field of 1.1 T. The large splitting between R^{++} and R^{--} suggests a large net magnetic moment across the entire sample. The spin asymmetry (SA) was described by $(R^{++}-R^{--})/(R^{++}+R^{--})$ (bottom panel). Open symbols and solid lines are experimental data and the results of best curve fitting, respectively. Errors bars represent the standard deviation. b) Schematic of a $(LMO_{18}/CRO_5)_9$ superlattice structure. c) The depth profiles of the nuclear scattering length density (nSLD) and the magnetic scattering length density (mSLD), were adopted to get the best curve fitting presented in (a).

reflectometry (PNR), a technique sensitive to spin asymmetry. As a function of wave vector transfer $q = 4\pi\sin\theta/\lambda$, **Figure 4**a (upper panel) shows the neutron reflectivity of $[(LMO)_{18}/(CRO)_5]_9$, obtained at 3.5 K with the neutron spin parallel (R^{++}) or antiparallel (R^{--}) to the magnetic field applied in the film plane, where θ is the incident angle of the neutron beam and λ is neutron wavelength. In addition to the regular intensity oscillation, a first-order Bragg reflection appears at $\sim q = 0.1$ Å^{-1}, implying the uniformity and sharp interfaces of the sample. The bottom panel of Figure 4a shows the calculated spin asymmetry SA = $(R^{++}-R^{--})/(R^{++}+R^{--})$ which carries information on the depth variation of the net magnetization across the SL. A best fitting is obtained for the PNR and SA data based on the model in Figure 4b,c which describes the nuclear scattering length density and magnetic scattering length density. Open symbols and solid lines in Figure 4a represent the experimental data and the results of best curve fitting, respectively. The good consistency between them indicates the nuclear and magnetic models in Figure 4c are reliable. The best fittings indicate an averaged magnetization of ~100 emu cm^{-3} (~0.8 μ_B/Ru) for the CRO layer and ~375 emu cm^{-3} (~3 μ_B/Mn) for the LMO layer. Notably, ~0.8 μ_B/Ru is nearly the highest magnetic moment available for the Ru^{4+} ions, i.e., CRO is in a collinear FM state. This is in sharp contrast to the proximity-induced canted antiferromagnetic state in heavy transition oxides such as $SrIrO_3$ and $CaIrO_3$ (~0.1 μ_B/Ir).[19–30] Moreover, the magnetic moments of Mn and Ru align along the same direction, implying a ferromagnetic coupling between them. Based on these results, we conclude with confidence that interface ferromagnetism is realized in PM CRO via interface engineering. Notably, this interface magnetism is comparable or even superior to the appreciative $SrRuO_3$ ($T_C \sim 150$ K and M~0.8-1.2 μ_B/Ru).[6–8,45,46,48]

The investigations of transport properties and PNR provide solid evidence on the establishment of a collinear FM order in the CRO layer of the SLs. A remaining issue that should be addressed is how the interface engineering works, resulting in the FM ground state for the CRO layer. As is well known, CRO owns itinerant 4d electrons and extended 4d orbits. This will facilitate a strong hybridization of the $3z^2 - r^2$ orbitals between neighboring Mn and Ru sites at the interfaces of the $(LMO_{18}/CRO_n)_8$ SLs, leading to molecular orbitals that mediate a magnetic exchange between CRO and LMO. This picture has been proven by density functional theory (DFT) calculations. Interfacial-hybridization-resulted redistribution of the partial density of states has been observed (Note 2 and Figure S5 of supporting information). Collinear FM state has been proven to be the ground state for the interfacial layer of CRO. The calculated magnetization is ~1.1 μ_B/Ru, in reasonable agreement with the experimental value (~0.8 μ_B/Ru).

2.4. Eightfold Magnetic Anisotropy

To get further knowledge about the magnetic phase, magnetic anisotropy (MA) of the interfacial layer is investigated. Unexpectedly, the MA is eightfold symmetric, in sharp contrast to the uniaxial anisotropy usually shown by the conventional (001)-oriented magnetic films. **Figure 5**a-c presents the anisotropic megnetoresistance AMR = $[R_{xx}(\theta)-R_{xx}(\theta = 90°)]/R_{xx}(\theta = 90°)$ for the

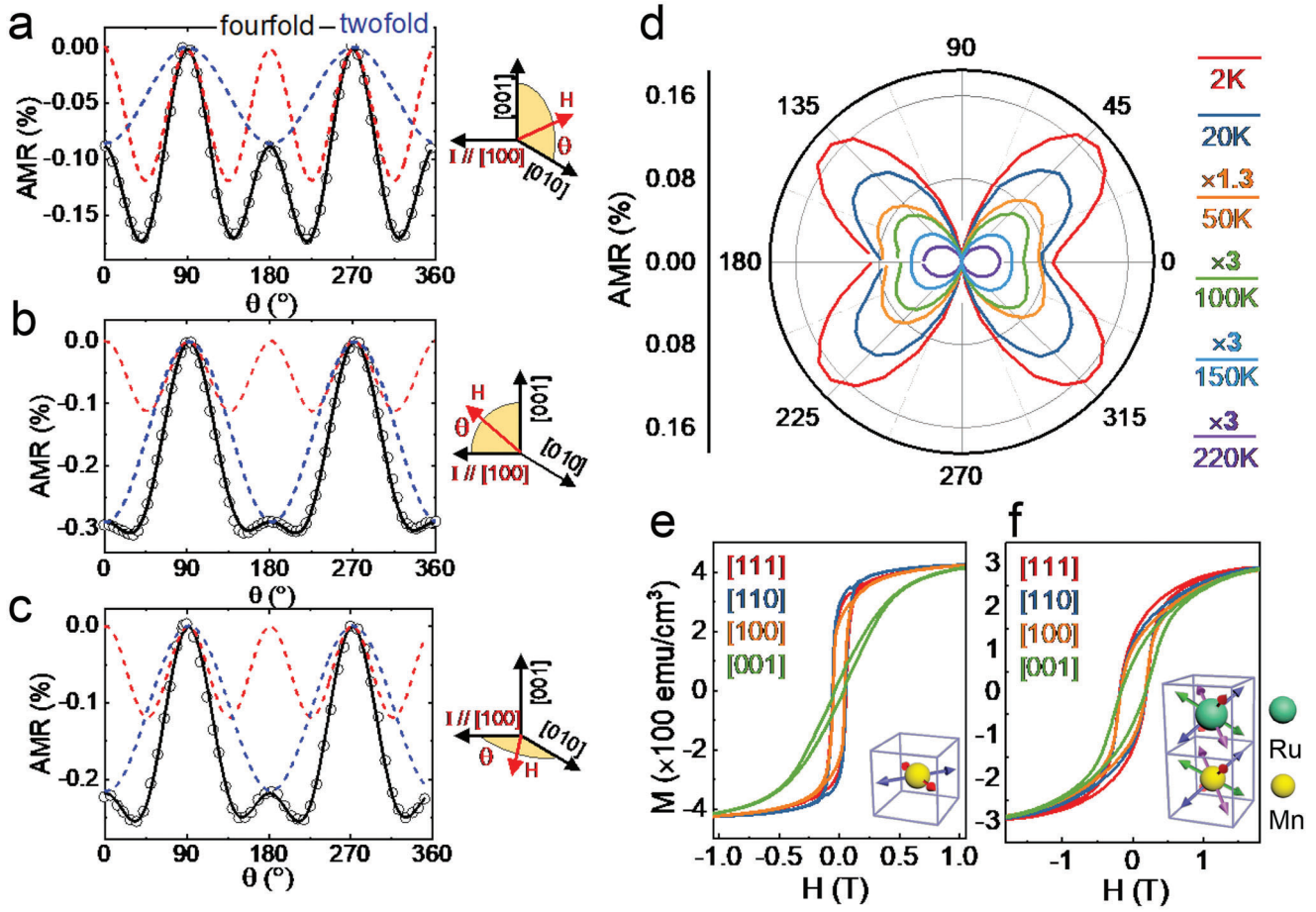

Figure 5. Eightfold-symmetric MA in the FM CRO layers of the SLs. a-c) AMR of the $[(LMO)_{18}/(CRO)_6]_8$ SL, obtained by rotating magnetic field in the (100), (010), and (001) crystalline planes, respectively. Black circles are experimental data. Black solid lines are the results of curve fitting. Red and blue dashed lines are fourfold and twofold components of the AMR, respectively. Right panels show the measurement geometry. The current is always along the [100] direction. θ denotes the angle between the applied field and the [010] direction in (a) and the angle between applied field and [100] direction in (b-c). The data were collected at $T = 5$ K and $H = 5$ T. d) Polar plots of AMR for the $(LMO_{18}/CRO_6)_8$ SL, measured at different temperatures adopting the same measurement geometry as Figure 5a. e) Magnetic hysteresis loops of LMO (56 nm) bare layer and $(LMO_{18}/CRO_6)_8$ SL, respectively, measured at $T = 5$ K.

sample of $(LMO_{18}/CRO_6)_8$, obtained by rotating magnetic field in the (100), (010), and (001) crystalline plane, respectively, where θ is the angle between the magnetic field and the [010]-, [100]-, or [100]-axis. The geometries for the measurements are shown in the right panels of the corresponding figures. At first glance, the AMR contains two components. One is fourfold symmetric (red dashed lines) and another is twofold symmetric (blue dashed lines). Thus, we fit the experimental data with the formula $AMR(\theta) = c_0 + c_{2fold} \times \cos(2\theta - \omega_{2fold}) + c_{4fold} \times \cos(4\theta - \omega_{4fold})$, where c_0 is the angle-independent MR, c_{2fold} and c_{4fold} are the amplitudes of the AMR with twofold and fourfold oscillations, respectively, ω_2 and ω_4 are the corresponding offset angles. Satisfactory agreement with experiment results is obtained by adopting suitable fitting parameters (Figure S5 of supporting information). As well documented, the fourfold symmetric AMR is closely related to ferromagnetism.[47] It exhibits four valleys in the [011], [01$\bar{1}$], [0$\bar{1}\bar{1}$], [0$\bar{1}$1] directions, respectively, when rotating the magnetic field in the (100) crystalline planes (Figure 5a). Notably, AMR valley appears when spin-flip scattering is minimal,[24,48] i.e., the preferred direction for spin alignments is ⟨011⟩ in the (100) plane. Similar analysis is conducted for the data in Figure 5b,c, revealing the preferred directions of ⟨101⟩ and ⟨110⟩ in the (010) and (001) planes, respectively. Moreover, the fourfold AMR observed in the three mutually orthogonal planes has the same amplitude (~0.13%). All these results strongly suggest that the interfacial phase has the magnetic easy axis along ⟨111⟩,[48] i.e., the MA of the interfacial CRO layer in the SL is eightfold symmetric.

Figure 5d is the polar plots of the AMR, obtained at different temperatures by rotating the magnetic field in the (100) plane. With the increase in temperature, an obvious transition is observed for the AMR, from mainly fourfold symmetry to completely twofold symmetry. As expected, the fourfold symmetric AMR appears only below T_C. Such a temperature dependence is a general feature of the AMR, also observed in the data obtained along the (001) and (010) crystalline planes (Figure S6 of supporting information). Therefore, the eightfold symmetric MA shows up only below T_C. As for the twofold symmetric AMR, it occurs

in the entire temperature range investigated (Figure S6 of supporting information), regardless of the magnetic state of the interfacial layer. It is usually ascribed to normal AMR or Lorentz scattering.[49–50]

It is worth noting that the⟨111⟩easy axis is a general feature of the $(LMO_{18}/CRO_n)_8$ SLs (Figure S7 of supporting information), though the amplitude of fourfold AMR, which characterizes the magnetic order, displays a monotonic decrease with the increase of the thickness of CRO (see Figure S8 of supporting information). Notably, the ⟨111⟩-directed magnetic anisotropy is robust, regardless of the strains in the samples on different substrates (Figure S9 of supporting information).

The eightfold symmetry could be ascribed to the combined effects of suppressed inter-planar Ru-Ru hopping, as suggested by the reduced conductivity of the SLs, and the distinct tilting/rotation of oxygen octahedra, as indicated by the data of Figure S10 in supporting information. According to Cui et al.,[48] these two factors combined will lead to a hybridization of Ru d_{xz} and Ru d_{yz} orbitals and a split into a pair of lower and upper Hubbard bands, resulting in correlation-driven orbital ordering thus eightfold ⟨111⟩ magnetic anisotropy.

In general, the conventional magnetic film is of uniaxial/biaxial anisotropy, exhibiting two/four stable spin directions. CRO presents a unusual eightfold symmetric MA with an easy axis of ⟨111⟩. This new MA has far-reaching scientific and technological implications, such as multistate memory devices with eight degenerate magnetic states in real space. Moreover, it can also generate *x*-, *y*- and *z*-direction polarized spin currents because of the coexistence of ferromagnetism and SOC in CRO.[2]

As a supplement, we would like to point out that the MA of the LMO layer is also eight-fold symmetric, as proved by the M-H curves measured in different directions (Figure 5f and Figure S11 in supporting information). It is interesting noting that the easy axis is [110] for the bare LMO film (Figure 5e). According to Yi et al.,[19] the reorientation of the magnetic easy axis in LMO could be caused by the sizeable SOC of CRO.

3. Conclusion

In summary, high quality (001)-oriented $(LMO_{18}/CRO_n)_8$ superlattices (n = 4, 6, 8, and 10 unit cells) have been fabricated and the magnetic proximity effects of LMO on CRO are investigated. Proximity-induced AHE is observed in the CRO layer, which is strong at low temperatures and remains sizable up to 180 K. Anomalous Hall conductivity is as large as 15 Ω^{-1} cm^{-1} and anomalous Hall angle is high as ~0.93%. Density functional theory calculations indicate the existence of avoid band crossings in the electronic band structure of the FM CRO layer, causing an enhancement in Berry curvature thus AHE. As evidenced by polarized neutron reflectometry, the CRO layers are in a collinear FM state, in sharp contrast to the proximity-induced canted antiferromagnetic state in heavy transition oxides such as $SrIrO_3$ and $CaIrO_3$. A further striking observation is the eightfold symmetry of the magnetic anisotropy of the (001)-$(LMO_{18}/CRO_n)_8$ superlattices, showing potential applications in the technology associated with multistate data storage (eight states are stored in one storage unit), spin-transfer or spin-orbit torque with a minimum of 71° spin switching (this will substantially reduce the critical current), and the generation of *z*-axis-directed spin current that is highly desired by electric switching of magnetization via spin-orbit torque.[2,51] The Curie temperature of the CRO layer is ~200 K. However, SLs with enhanced Curie temperatures are required by practical applications. A viable approach may be to find or synthesize a FM insulator which has a high Curie temperature and exhibit an epitaxial growth on CRO. The present work clearly shows that a heavy transition metal oxide with strong SOC can be driven into a collinear FM state by the magnetic proximity effect, demonstrating the great potential of interface engineering in tailoring the functionality of complex oxides.

4. Experimental Section

Sample Fabrication and Characterization: $(LMO_{18}/CRO_n)_8$ superlattices (SLs) composed of alternately stacked LMO (fixed thickness of 18 uc) and CRO (n = 4, 6, 8, and 10 unit cells) with 8 repetitions were epitaxially grown on (001)-oriented $(LaAlO_3)_{0.3}(SrAl_{0.5}Ta_{0.5}O_3)_{0.7}$ (LSAT) substrates by pulse laser deposition (KrF Excimer laser, wavelength = 248 nm). During the deposition process, the substrate temperature was kept at 700 °C and the oxygen atmosphere was fixed to 30 Pa. The fluence of the laser pulse was 2 J cm^{-2} and the repetition rate was 2 Hz. Before the fabrication of the SLs, two control samples, a CRO and a LMO bare film with a relatively thick thickness, were prepared. The exact film thickness was then determined by the technique of small-angle X-ray reflectivity (XRR). Since the number of laser pulses has been recorded during the experiment, the growth rate, i.e., how many laser pulses are required by one unit cell CRO or LMO layer, can be accurately determined. Here relatively thick control films were adopted to improve the precision of the growth rate. After these experiments, the $(LMO_{18}/CRO_n)_8$ superlattices were prepared to adopt the calibrated growth rate for the CRO and LMO layers, i.e., the layer thickness was controlled by the number of laser pulses.

Polarized Neutron Reflectometry (PNR): PNR experiments were performed at MR beamline of the Chinese Spallation Neutron Source (CSNS). The samples were field-cooled and measured at 1.1 T along the in-plane direction. PNR measurements were carried out at 3.5 K in the specular reflection geometry with wave vector transfer (q) perpendicular to the surface plane. The neutron reflectivity was recorded as a function of q for the spin-up (R^{++}) and spin-down (R^{--}) polarized neutrons. The difference between R^{++} and R^{--} was calculated as the spin asymmetry [SA = $(R^{++} - R^{--})/(R^{++} + R^{--})$]. The PNR data were fitted using the GenX software.

Supporting Information

Supporting Information is available from the Wiley Online Library or from the author.

Acknowledgements

J.Z. and X.C. contributed equally to this work. This work has been supported by the National Key R&D Program of China (Grants No. 2022YFA1403302, No. 2021YFA1400300, No. 2020YFA0711502, No. 2019YFA0704904, and No. 2018YFA0305704), the Science Center of the National Science Foundation of China (Grant No. 52088101), the National Natural Science Foundation of China (Grants No. 11934016, No. 92263202, No. 12274443, No. 12104029, No. 51972335, No. 62122008, No. 61971024, No. 12004022 and No. 12104027), and Strategic Priority Research Program (B) of the Chinese Academy of Sciences (XDB33030200). J.R.S. is thankful for the support of the Project for Innovative Research Team of the National Natural Science Foundation of China (Project No. 11921004).

Conflict of Interest

The authors declare no conflict of interest.

Data Availability Statement

The data that support the findings of this study are available from the corresponding author upon reasonable request.

Keywords

eightfold magnetic anisotropy, ferromagnetic states, oxide superlattices, proximity effect, strong anomalous Hall effect

Received: July 19, 2023
Published online: August 22, 2023

[1] V. P. A. Davidson, W. S. Aljuaid, P. M. Haney, X. Fan, *Phys. Lett. A* **2020**, *384*, 126228.
[2] V. P. Amin, J. Li, M. D. Stiles, P. M. Haney, *Phys. Rev. B* **2019**, *99*, 220405(R).
[3] S. C. Baek, V. P. Amin, Y.-W. Oh, G. Go, S.-J. Lee, G.-H. Lee, K.-J. Kim, M. D. Stiles, B.-G. Park, K.-J. Lee, *Nat. Mater.* **2018**, *17*, 509.
[4] P. M. Haney, M. D. Stiles, *Phys. Rev. Lett.* **2010**, *105*, 126602.
[5] G. Koster, L. Klein, W. Siemons, G. Rijnders, J. S. Dodge, C. B. Eom, D. H. A. Blank, M. R. Beasley, *Rev. Mod. Phys.* **2012**, *84*, 253.
[6] S. Thomas, B. Kuiper, J. Hu, J. Smit, Z. Liao, Z. Zhong, G. Rijnders, A. Vailionis, R. Wu, G. Koster, J. Xia, *Phys. Rev. Lett.* **2017**, *119*, 177203.
[7] K. Takiguchi, Y. K. Wakabayashi, H. Irie, Y. Krockenberger, T. Otsuka, H. Sawada, S. A. Nikolaev, H. Das, M. Tanaka, Y. Taniyasu, H. Yamamoto, *Nat. Commun.* **2020**, *11*, 4969.
[8] W. Lin, L. Liu, Q. Liu, L. Li, X. Shu, C. Li, Q. Xie, P. Jiang, X. Zheng, R. Guo, Z. Lim, S. Zeng, G. Zhou, H. Wang, J. Zhou, P. Yang, S. J. P. Ariando, X. Xu, Z. Zhong, Z. Wang, J. Chen, *Adv. Mater.* **2021**, *33*, 2101316.
[9] J. Wei, H. Zhong, J. Liu, X. Wang, F. Meng, H. Xu, Y. Liu, X. Luo, Q. Zhang, Y. Guang, J. Feng, J. Zhang, L. Yang, C. Ge, L. Gu, K. Jin, G. Yu, X. Han, *Adv. Funct. Mater.* **2021**, *31*, 2100380.
[10] H. Y. Hwang, Y. Iwasa, M. Kawasaki, B. Keimer, N. Nagaosa, Y. Tokura, *Nat. Mater.* **2012**, *11*, 103.
[11] S. Okamoto, A. J. Millis, *Nature* **2004**, *428*, 630.
[12] P. Yu, J. S. Lee, S. Okamoto, M. D. Rossell, M. Huijben, C. H. Yang, Q. He, J. X. Zhang, S. Y. Yang, M. J. Lee, Q. M. Ramasse, R. Erni, Y. H. Chu, D. A. Arena, C. C. Kao, L. W. Martin, R. Ramesh, *Phys. Rev. Lett.* **2010**, *105*, 027201.
[13] J. Matsuno, K. Ihara, S. Yamamura, H. Wadati, K. Ishii, V. V. Shankar, H.-Y. Kee, H. Takagi, *Phys. Rev. Lett.* **2015**, *114*, 247209.
[14] J. A. Bert, B. Kalisky, C. Bell, M. Kim, Y. Hikita, H. Y. Hwang, K. A. Moler, *Nat. Phys.* **2011**, *7*, 767.
[15] M. Verissimo-Alves, P. García-Fernández, D. I. Bilc, P. Ghosez, J. Junquera, *Phys. Rev. Lett.* **2012**, *108*, 107003.
[16] M. Gibert, P. Zubko, R. Scherwitzl, J. Iniguez, J. Triscone, *Nat. Mater.* **2012**, *11*, 195.
[17] J. Matsuno, N. Ogawa, K. Yasuda, F. Kagawa, W. Koshibae, N. Nagaosa, Y. Tokura, M. Kawasaki, *Sci. Adv.* **2016**, *2*, e1600304.
[18] X. Liu, W. Song, M. Wu, Y. B. Yang, Y. Yang, P. Lu, Y. Tian, Y. Sun, J. Lu, J. Wang, D. Yan, Y. Shi, N. X. Sun, Y. Sun, P. Gao, K. Shen, G. Z. Chai, S. P. Kou, C.-W. Nan, J. X. Zhang, *Nat. Commun.* **2021**, *12*, 5453.
[19] D. Yi, J. Liu, S.-L. Hsu, L. Zhang, Y. Choi, J.-W. Kim, Z. Chen, J. D. Clarkson, C. R. Serrao, E. Arenholz, P. J. Ryan, H. Xu, R. J. Birgeneau, R. Ramesh, *Proc. Natl. Acad. Sci. USA* **2016**, *113*, 6397.
[20] M.-W. Yoo, J. Tornos, A. Sander, L.-F. Lin, N. Mohanta, A. Peralta, D. Sanchez-Manzano, F. Gallego, D. Haskel, J. W. Freeland, D. J. Keavney, Y. Choi, J. Strempfer, X. Wang, M. Cabero, H. B. Vasili, M. Valvidares, G. Sanchez-Santolino, J. M. Gonzalez-Calbet, A. Rivera, C. Leon, S. Rosenkranz, M. Bibes, A. Barthelemy, A. Anane, E. Dagotto, S. Okamoto, S. G. E. te Velthuis, J. Santamaria, J. E. Villegas, *Nat. Commun.* **2021**, *12*, 3283.
[21] J. W. Kim, Y. Choi, S. H. Chun, D. Haskel, D. Yi, R. Ramesh, J. Liu, P. J. Ryan, *Phys. Rev. B* **2018**, *97*, 094426.
[22] G. A. Ovsyannikov, T. A. Shaikhulov, K. L. Stankevich, Y. Khaydukov, N. V. Andreev, *Phys. Rev. B* **2020**, *102*, 144401.
[23] Y. Zhang, Y. Z. Luo, L. Wu, M. Suzuki, Q. Zhang, Y. Hirata, K. Yamagami, K. Takubo, K. Ikeda, K. Yamamoto, A. Yasui, N. Kawamura, C. Lin, K. Koshiishi, X. Liu, J. Zhang, Y. Hotta, X. R. Wang, A. Fujimori, Y. Lin, C. Nan, L. Shen, H. Wadati, *Phys. Rev. Res.* **2020**, *2*, 33496.
[24] A. K. Jaiswal, D. Wang, V. Wollersen, R. Schneider, M. Le Tacon, D. Fuchs, *Adv. Mater.* **2022**, *34*, 2109163.
[25] J. Nichols, X. Gao, S. Lee, T. L. Meyer, J. W. Freeland, V. Lauter, D. Yi, J. Liu, D. Haskel, J. R. Petrie, E.-J. Guo, A. Herklotz, D. Lee, T. Z. Ward, G. Eres, M. R. Fitzsimmons, H. N. Lee, *Nat. Commun.* **2016**, *7*, 12721.
[26] S. Okamoto, J. Nichols, C. Sohn, S. Y. Kim, T. W. Noh, H. N. Lee, *Nano Lett.* **2017**, *17*, 2126.
[27] Z. S. Lim, C. Li, Z. Huang, X. Chi, J. Zhou, S. Zeng, G. J. Omar, Y. P. Feng, A. Rusydi, S. J. Pennycook, T. Venkatesan, A. Ariando, *Small* **2020**, *16*, 2004683.
[28] M. Vagadia, J. Sahoo, A. Kumar, S. Sardar, T. M. Tank, D. S. Rana, *Phys. Rev. B* **2023**, *107*, 064420.
[29] M. Vagadia, S. Sardar, T. Tank, S. Das, B. Gunn, P. Pandey, R. Hübner, F. Rodolakis, G. Fabbris, Y. Choi, D. Haskel, A. Frano, D. S. Rana, *Phys. Rev. B* **2022**, *105*, L020402.
[30] Z. S. Lim, C. Li, X. Chi, G. J. Omar, H. H. Ma, Z. Huang, S. Zeng, P. Yang, T. Venkatesan, A. Rusydi, S. J. Pennycook, A. Ariando, *Nano Lett.* **2020**, *20*, 1890.
[31] Z. Hu, H. von Lips, M. S. Golden, J. Fink, *Phys. Rev. B* **2000**, *61*, 5262.
[32] Z. Fang, N. Nagaosa, K. S. Takahashi, A. Asamitsu, R. Mathieu, T. Ogasawara, H. Yamada, M. Kawasaki, Y. Tokura, K. Terakura, *Science* **2003**, *302*, 92.
[33] A. Gupta, T. R. McGuire, P. R. Duncombe, M. Rupp, J. Z. Sun, W. J. Gallagher, G. Xiao, *Appl. Phys. Lett.* **1995**, *67*, 494.
[34] E. Hua, L. Si, K. Dai, Q. Wang, H. Ye, K. Liu, J. Zhang, J. Lu, K. Chen, F. Jin, L. Wang, W. Wu, *Adv. Mater.* **2022**, *34*, 2206685.
[35] N. Nagaosa, J. Sinova, S. Onoda, A. H. MacDonald, N. P. Ong, *Rev. Mod. Phys.* **2010**, *82*, 1539.
[36] S. Onoda, N. Sugimoto, N. Nagaosa, *Phys. Rev. B* **2008**, *77*, 165103.
[37] P. Matl, N. P. Ong, Y. F. Yan, *Phys. Rev. B* **1998**, *57*, 10248.
[38] Y. Lyanda-Geller, S. H. Chun, M. B. Salamon, P. M. Goldbart, P. D. Han, *Phys. Rev. B* **2001**, *63*, 184426.
[39] J. Zhang, H. Zhang, H. Zhang, Y. Ma, X. Chen, F. Meng, S. Qi, Y. Chen, F. Hu, Q. Zhang, B. Liu, B. Shen, W. Zhao, W. Han, J. Sun, *ACS Appl. Mater. Interfaces* **2020**, *12*, 28775.
[40] R. P. Khosla, J. R. Fischer, *Phys. Rev. B* **1970**, *2*, 4084.
[41] Y. J. Zeng, L. M. Pereira, M. Menghini, K. Temst, A. Vantomme, J. P. Locquet, C. Van Haesendonck, *Nano Lett.* **2012**, *12*, 666.
[42] H. R. Zhang, X. Yan, H. Zhang, F. Wang, Y. Gu, X. Ning, T. Khan, R. Li, Y. S. Chen, W. Liu, S. Wang, B. G. Shen, J. R. Sun, *Phys. Rev. B* **2018**, *97*, 155150.
[43] K. Yosida, *Phys. Rev.* **1957**, *107*, 396.
[44] S. Li, Q. Zhang, S. Lin, X. Sang, R. F. Need, M. A. Roldan, W. Cui, Z. Hu, Q. Jin, S. Chen, J. Zhao, J.-O. Wang, J. Wang, M. He, C. Ge, C. Wang, H.-B. Lu, Z. Wu, H. Guo, X. Tong, T. Zhu, B. Kirby, L. Gu, K.-j. Jin, E.-J. Guo, *Adv. Mater.* **2021**, *33*, 2001324.
[45] K. Terai, T. Ohnishi, M. Lippmaa, H. Koinuma, M. Kawasaki, *Jpn. J. Appl. Phys.* **2004**, *43*, L227.
[46] C. B. Eom, R. J. Cava, R. M. Fleming, J. M. Philips, R. B. van Dover, J. H. Marshall, J. W. P. Hsu, J. J. Krajewski, W. F. Peck Jr., *Science* **1992**, *258*, 1766.
[47] Y. Dai, Y. W. Zhao, L. Ma, M. Tang, X. P. Qiu, Y. Liu, Z. Yuan, S. M. Zhou, *Phys. Rev. Lett.* **2022**, *128*, 247202.

[48] Z. Cui, A. J. Grutter, H. Zhou, H. Cao, Y. Dong, D. A. Gilbert, J. Wang, Y.-S. Liu, J. Ma, Z. Hu, J. Guo, J. Xia, B. J. Kirby, P. Shafer, E. Arenholz, H. Chen, X. Zhai, Y. Lu, *Sci. Adv.* **2020**, *6*, eaay0114.
[49] R. Ramos, S. K. Arora, I. V. Shvets, *Phys. Rev. B* **2008**, *78*, 214402.
[50] A. Annadi, Z. Huang, K. Gopinadhan, X. R. Wang, A. Srivastava, Z. Q. Liu, H. H. Ma, T. P. Sarkar, T. Venkatesan, Ariando, *Phys. Rev. B* **2013**, *87*, 201102(R).
[51] Y. Ou, Z. Wang, C. S. Chang, H. P. Nair, H. Paik, N. Reynolds, D. C. Ralph, D. A. Muller, D. G. Schlom, R. A. Buhrman, *Nano Lett.* **2019**, *19*, 3663.